SAND2000-8526C

Effect of electron transport properties on unipolar CdZnTe radiation detectors: LUND, SpectrumPlus, and coplanar grid

E. Y. Lee and R. B. James

Sandia National Laboratories

Livermore, CA 94550

Abstract

Device simulations of (1) the laterally-contacted-unipolar-nuclear detector (LUND), (2) the SpectrumPlus, (3) and the coplanar grid made of $Cd_{0.9}Zn_{0.1}Te$ (CZT) were performed for ^{137}Cs irradiation by 662.15 keV gamma-rays. Realistic and controlled simulations of the gamma-ray interactions with the CZT material were done using the MCNP4B2 Monte Carlo program, and the detector responses were simulated using the Sandia three-dimensional multielectrode simulation program (SandTMSP). The simulations were done for the best and the worst expected carrier mobilities and lifetimes of currently commercially available CZT materials for radiation detector applications. For the simulated unipolar devices, the active device volumes were relatively large and the energy resolutions were fairly good, but these performance characteristics were found to be very sensitive to the materials properties. The internal electric fields, the weighting potentials, and the charge induced efficiency maps were calculated to give insights into the operation of these devices.

I. Introduction

The unipolar radiation detectors made of semi-insulating $Cd_{0.9}Zn_{0.1}Te$ (CZT) [Ref. 1,2] have recently received much attention, due to their potential for improved gamma-ray detection sensitivity and energy resolution [3-6]. Because the electron mobilities are ~ 20 times larger than the hole mobilities and because the electron lifetimes are at least ~ 10 times longer than the hole lifetimes in these materials [7,8], these unipolar devices are designed to depend only on the electron's transport properties. However, because of the unknown variation in the starting detector materials, the high cost of materials and fabrication, and the relatively complex geometries and operating conditions that are characteristic of these unipolar detector designs, quantitative experimental determination of their active volume and energy resolution are typically extremely difficult. And it is just as difficult to determine how robust these performance characteristics are with respect to the inevitable variation of the of the carrier transport properties.

A solution to these difficult tasks is to use validated computer programs for the simulation of these devices. A device simulation can give the total control of the device and materials parameters and, in addition, it can allow the examination of all device functions. We have performed device simulations of three recently developed unipolar detectors made of $Cd_{0.9}Zn_{0.1}Te$: (1) the laterally-contacted-unipolar-nuclear detector (LUND) [Ref. 3,4], (2) the SpectrumPlus [Ref. 5], and (3) the coplanar grid [6]. We did simulations for the best and worst CdZnTe materials that are currently commercially available. Full three-dimensional simulations were performed for both the interaction of the gamma-rays with CZT and for the detector response. The MCNP4B2 program [9]

DISCLAIMER

DISCLAIMER

Portions of this document may be illegible in electronic image products. Images are produced from the best available original document.

was used for realistic and controlled interaction of gamma-rays with the detector. The internal electric fields, the weighting potentials, the charge induced efficiency maps, and the pulse height spectra were calculated using the SandTMSP [10]. The results show that the unipolar designs give relatively large active device volumes and fairly good energy resolutions. However, despite the unipolar designs, these performance characteristics were found to be very sensitive to the materials properties and we conclude that the best available materials are necessary to make the best detectors.

II. Simulation geometry and detector dimensions and biases

In this section, we describe the structure, dimensions, and voltage biases of the simulated detectors. For all the detectors, the geometry shown in Fig. 1 was used, and irradiation by a 1-mm-diameter ^{137}Cs was assumed to provide monoenergetic gamma-rays at 662.15 keV. In all cases, the voltage biases consistent with maximum internal electric field of 100 V/mm were chosen, because the electrons in CdZnTe reaches saturation velocity of ~ 10^7 cm/sec at this field [11] and also because the leakage current (due to the surface and the bulk) through the material becomes appreciable at this field. In addition, all the detectors were oriented looking at the source with a face without any electrode.

The LUND had dimensions of 10x10x2 mm^3. Its cathode and the anode were placed at the two 10x2 mm^2 faces. In addition, there was a guard ring 0.1 mm thick located 1.8 mm from the anode. The guard ring was parallel to the anode and was grounded. The anode and the cathode were at 180 V and –810 V, respectively. Schematic representations of all three simulated unipolar devices are shown in Fig. 2.

The SpectrumPlus detector was a cubic detector of dimensions 5x5x5 mm^3. Its cathode was located on one face of the cube. On the opposite face, a circular anode having 0.3 mm radius was placed at the center. One the same face, a guard structure was placed around the anode. Its inner diameter was 1.5 mm and it extended to the edge of the face. The guard was grounded, and the anode and the cathode were at 120 V and –380 V.

The coplanar grid was a cubic detector of dimensions 5x5x5 mm^3. Its cathode was located on one face of the cube. On the opposite face, four interdigitated strips are placed as the collecting grid and the noncollecting grid. The strips were 0.6 mm thick and spaced 0.6 mm apart. The two noncollecting grid strips were grounded, and the two collecting grid strips were at 60 V, and the cathode was biased at –400 V.

III. Method of Computation

The simulation used several subprograms of the SandTMSP and also of the MCNP4B2. The MCNP4B2 program allowed realistic and controlled simulation of photon transport in CZT, and it also allowed detailed analysis of the transport. The detailed photon transport model in MCNP4B2 took into account incoherent scattering (Compton scattering), coherent scattering (Thompson scattering), single florescence event, double florescence event, terminal capture event, and multiple scattering. As the radiation source in the simulation, a 1-mm-diameter sphere containing ^{137}Cs was placed 6 cm away from the center of a side face of the detector. The embedding source material was plastic, and the source and the detector were surrounded by air. The Monte Carlo simulation tracked each photon from the source and recorded (1) the energy deposited, (2) the location of deposition, (3) the time of deposition, (4) the type of scattering, and (5)

any secondary photons that were created. Secondary photons were tracked further. Secondary electrons either deposited all their energy at once or deposited part of their energy and created secondary photons by bremsstrahlung.

The internal electrostatic fields of the detectors and the weighting potentials for the signal electrodes were calculated using the SandTMSP, in which the Gaussian successive over-relaxation method [12] was used to iteratively solve for the three-dimensional fields. With each successive iteration, the total energy of the field decreased and the field converged everywhere. The actual potential field was a sum of the weighting potentials weighted by the biases on the respective electrodes. Fixed boundary conditions were used, and these were chosen to minimize the total energy. The details were sensitive to the boundary conditions, but our main conclusions were not.

For the computation of the internal electric field, we assumed that there was no built-in field within the crystal. This is consistent with the known high resistivities of these semi-insulating materials and hence also with the low free carrier concentrations. There have been reports of intensified electric field near the cathode, as seen by infrared imaging using the electro-optic effect [14], however the results are controversial due the possibility of photoionization of deep traps during the measurements [15].

The charge induced efficiency maps (CIEM's) were calculated using the SandTMSP, using a transport model described previously [4]. In this model, the induced charge is

$$Q(\mathbf{r}_0,t) = \int_0^t dt \begin{pmatrix} \mu_e Q_e(t)\mathbf{E}_i^w(\mathbf{r}_e(\mathbf{r}_0,t)) \bullet \mathbf{E}(\mathbf{r}_e(\mathbf{r}_0,t)) + \\ \mu_h Q_h(t)\mathbf{E}_i^w(\mathbf{r}_h(\mathbf{r}_0,t)) \bullet \mathbf{E}(\mathbf{r}_h(\mathbf{r}_0,t)) \end{pmatrix}, \quad \text{Eq. (1)}$$

where

$$Q_e(t) = Q_0 \exp(-\frac{t}{\tau_e}), \qquad \text{Eq. (2)}$$

$$Q_h(t) = Q_0 \exp(-\frac{t}{\tau_h}), \qquad \text{Eq. (3)}$$

and Q_0 is the initial charge photogenerated by the gamma-ray at $t = 0$ and at the position $\mathbf{r}_0$, τ_e is the electron lifetime, τ_h is the hole lifetime, μ_e is the electron mobility, μ_h is the hole mobility, $\mathbf{r}_{e,h}(\mathbf{r}_0,t)$ is the position of the electron and hole charges as a function of time, the total electric field is **E**, and the weighting potential for the *i*th electrode is $\mathbf{E}_i^w$. In the model, because carrier diffusion is ignored, the charge carriers move along stream lines, with the velocities and charges determined by the mobilities and the lifetimes of the carriers. Since detailed treatment of trapping and detrapping is not done, the mobilities and the lifetimes are *effective* values that describes the net motion of the charge carriers.

For the planar detector, $\mathbf{E} = \mathbf{E}_i^w$, within a possible sign factor, and **E** is a scalar independent of time and position. In this case, by simple integration of Eq. (1), one gets the Hecht relation. For a unipolar device, $\mathbf{E} \neq \mathbf{E}_i^w$ and $\mathbf{E}_i^w$ is localized and it has a strong spatial dependence. Therefore, instead of the Hecht relation, the general expression, shown in Eq. (1), must be used. In general, this evaluation requires numerical methods and, in our case, we have done this using the SandTMSP. For the LUND, the SandTMSP was previously found to realistically simulate the detector response, and it was used to optimize the device structure [4,13]. In SandTMSP, the statistical noise associated with the Fano factor is ignored and electronic noise of 1 keV was convoluted with the simulated pulse height spectra. The shaping time for the spectroscopy amplifier was assumed to be long enough to ensure that the ballistic deficit did not occur.

For the electron and hole mobilities and lifetimes, we used values typical of the best and the worst currently commercially available CZT. These parameters are shown in Table I.

IV. Interaction of ^{137}Cs gamma-rays with CZT

The 662.15 keV gamma-rays from ^{137}Cs interact with CZT primarily by Compton scattering. Additional scattering mechanisms are Thompson scattering and photoelectric absorption with the emission of 0, 1, or 2 photons. Secondary photons resulting from these events can undergo the same processes. By the Monte Carlo simulation using the MCNP4B2, we find the attenuation length of 662.15 keV gamma-rays in $Cd_{0.9}Z_{0.1}Te$ to be ~ 2.0 cm. We define the attenuation length precisely as the depth for 1/e attenuation of the *primary unscattered* gamma-ray flux in a material. If one counted the total flux, including the secondary gamma-rays, the attenuation length would be larger. Fig. 3 gives the percentage of various events for the primary and secondary gamma-rays for a 5x5x5 mm^3 CZT detector. It can be seen that 83% of the primary 662.15 keV gamma-rays interacting the detector do so by Compton scattering. Photoelectric absorption (terminal capture events and florescence events) is only 10 %. The secondary photons that have lower energy are more likely to undergo photoelectric absorption, but these do not contribute to the photoelectric peak in a pulse height spectrum.

Fig. 4 shows a spectrum of the total energy deposited in a 10x10x2 and 5x5x5 mm^3 CZT in the geometry shown in Fig. 1 by a ^{137}Cs source. If one had a perfect CZT detector with an infinite good energy resolution and 100% active volume, then the best pulse height spectrum one can obtain is such a spectrum. The main features are the photoelectric peak at the highest energy, the x-ray escape peak immediately below it, and the Compton edge. We shall see in a following section how well the unipolar detectors behave in comparison to this ideal case.

V. Computational results and discussion

In this section, we will examine the internal electrostatic field, the weighting potentials, the charge induced efficiency maps (CIEM's), and the pulse height spectra of the LUND, the SpectrumPlus and the coplanar grid. The internal electrostatic fields and the weighting potentials are independent of the carrier transport properties. It only depends on the dielectric constant of the material, which is known to be 10. The CIEM's and the pulse height spectra are dependent on both the carrier mobilities and lifetimes.

V.A. The total internal electrostatic potential

The internal electrostatic potential field determines the motion of the charge carriers within the detector, and these are shown in Fig. 5. From the actual three-dimensional fields, the cross sections through the middle of the detectors were taken. In fig. 5, the contour lines separate every ~ 50 V in the potential field. The motion of the charge carriers follows the electric field lines that are perpendicular to the contour lines.

It can be seen that the field inside the LUND is fairly uniform and hence that most electrons within the detector travel straight to the anode on the right. For this particular LUND structure and biases, the presence of the guard does not significantly disturb the potential field. In the SpectrumPlus, the field is uniform in most of the detector, but it is intensified near the anode. Electrons near the side faces of the SpectrumPlus travel to the guard, whereas the electrons near the center travel toward the anode. In the coplanar grid, the field is uniform in most of the detector, but it has some nonuniformity near the grids. The motion of the electrons in the detector is mostly straight toward the strips.

It is notable that significant fractions of the electrons in the SpectrumPlus and in the coplanar grid travel to the guard and to the noncollecting grid, respectively. This also

happens in the LUND, but to a less extent. This is important, because those electrons induce net zero signal on the signal electrodes. For the optimization of these devices, the internal potential fields need to be engineered to minimize the number of these electrons traveling to the guard structure or to the noncollecting grid.

V.B. The weighting potential for the anode

The weighting potential an electrode is the potential when that electrode is set at 1 V and all the other electrodes are set at 0 V. In the absence of trapping, it can be shown that the signal induced on that electrode by the motion of the charge carriers is proportional to the change of the weighting potential during the motion. This is known as Ramo's theorem. If the weighting potential is localized, as is the case for the unipolar devices, then the effects of trapping are mitigated and Ramo's theorem still holds to a good approximation. In a well designed unipolar device, the weighting potential is strongly localized near the anode. The weighting potentials for the three unipolar devices are shown in Fig. 6.

In all cases, it can be seen that the weighting potential is indeed localized near the anode. For the LUND, the weighting potential is effectively localized between the grid and the anode. For the SpectrumPlus, the weighting potential is localized as 1/r, with sharper localization in the plane of the anode by the guard. For the coplanar grid, the weighting potential varies as log(r). This is not very localized, however, for the coplanar grid, one takes the difference between the collecting and the noncollecting grid as the signal, and this gives an effective localization.

V.C. Charge induced efficiency maps

The charge induced efficiency maps (CIEM's) show the spatial response of the detectors. In Fig. 7 is shown the CIEM's for the three unipolar devices. The lighter areas indicate the larger responses, meaning high charge collection efficiencies and hence higher channels in the pulse height spectra. The dark areas indicate low or zero charge collection efficiencies. The active device volumes correspond to the lighter areas. The CIEM's shown in Fig. 7 were calculated for the best expected materials parameters shown in Table 1.

There is no standard definition of the active device region for the unipolar devices. To allow a comparative analysis, let us define it here as the volume consisting of regions of the detector that give charge collection efficiencies within 30% of the maximum. For ^{137}Cs, the Compton edge is 30% below the photoelectric peak, and, therefore, the practical meaning of the active volume is the volume giving counts above the Compton edge in a pulse height spectrum. Table 2 shows the active volumes for the three detectors, for the best and the worst expected materials. It can be seen that active volumes are considerably smaller for the worst materials.

In the LUND, the active device region is a fairly large area between the cathode and the grid. For the SpectrumPlus, the active device region is confined to a cylindrical volume ending at the anode, and this is due to the trajectory of the electrons within the device. For the coplanar grid, the active device volumes are parallelepiped regions ending at the collecting grids. As in the SpectrumPlus, only the electrons from these regions end up at the collecting grid.

For the coplanar grid, one may note that two active device regions do not have the same spatial dependence. This is due to the asymmetry of the internal potential fields, and this is a known effect that can be eliminated by carefully designing the grid spacing, pitch, and symmetry [16].

V.D. Pulse height spectra

The pulse height spetra for the three unipolar devices are shown in Fig. 8. The energies of gamma-rays are determined from the photoelectric peak channels in the pulse height spectra. In contrast to the ideal spectra shown in Fig. 4, realistic spectra have broadened photoelectric peaks that also have low counts. In addition, the low energy counts are larger. These features can be directly attributed to the inhomogeneous spatial response of the detector that can be seen in the CIEM's shown in Fig. 7. The simulations were done for the best and the worst expected materials parameters shown in Table 1.

It can be seen from Fig. 8 that the LUND device performs quite well for the best material. However, for the worst expected material, the photoelectric peak nearly disappears. The spectrum becomes comparable to that of a conventional planar detector (not shown). Similar trends can be seen for the other detectors. For both the SpectrumPlus and the coplanar grid, the photoelectric peak can not been in the worst material. For the best materials, the photoelectric peak, although relatively broad, can be seen. By the optimization of the biases and the detector dimensions, one can significantly improve the energy resolution of these devices, as we have shown for the LUND [13]. Also, by using shorter shaping times for the spectroscopy amplifier, one can also sharpen the photoelectric peak, at the price of introducing ballistic deficit which reduces the overall signal strength.

VI. Conclusion

In conclusion, we have performed realistic and controlled device simulation of the laterally-contacted-unipolar-nuclear detector, SpectrumPlus, and the coplanar grid made of $Cd_{0.9}Zn_{0.1}Te$ (CZT) for ^{137}Cs irradiation by 662.15 keV gamma-rays. We achieved realistic Monte Carlo simulation of the gamma-energy interaction with the CZT detector using the MCNP4B2, and we used the SandTMSP for the three-dimensional computation of the detector responses. The internal potential fields of the detectors were computed and they showed the trajectory of the photogenerated carriers within the detectors. The weighting potentials for the anodes were calculated, to show their degree of localization. The charge induced efficiency maps were computed, to show the spatially resolved detector responses. All three detectors were found to have unique spatial response functions and different active volumes. In comparison to the conventional planar detector in which the active device volume is only a few percent of the total volume and corresponds to a small region close to the cathode, the unipolar devices had larger active regions. In addition, the pulse height spectra for the best and the worst expected materials were computed. These materials parameters were taken from literature, from studies of currently commercially available materials. For all three detectors, the photoelectric peak was not even visible for the worst expected material. The best materials were necessary to get the best spectra, indicative of the best performance. These results show that, despite the relatively large active device volumes, for the best performance, the unipolar devices must be made from the best available materials.

Acknowledgement

We gratefully acknowledge the support of the US DOE Office of Research and Development, in the Office of Nuclear Nonproliferation and National Security, NN-20. This work has been done under U. S. Department of Energy contract no. DE-AC04-94AL85000. At Sandia National Laboratories, we acknowledge J. C. Lund, B. Brunett and J. Van Scyoc III for useful discussions during the earlier part of this work.

List of References

1. R. B. James, B. Brunett, J. Heffelfinger, J. van Scyoc, J. C. Lund, F. P. Doty, C. L. Lindgren, R. W. Olsen, E. Cross, H. Hermon, H. Yoon, N. Hilton, M. Schieber, E. Y. Lee, J. Toney, E.T. E. Schlesinger, M. Goorsky, W. Yao, H. Chen, and A. Burger, J. of Electron. Mater. **27**, 788(1998).

2. C. Szeles and E. E. Eissler, "Current Issues of High-Pressure Bridgeman Growth of Semi-insulating CdZnTe," Materials Research Society Symposium Proceedings. Semiconductors for Room-Temperature Radiation Detector Applications II, Vol. **487**, edited by R. B. James, T. E. Schlesinger, P. Siffert, W. Dusi, M. R. Squillante, M. O'Connell, and M. Cuzin (Materials Research Society, Warrendale, Pennsylvania, 1998), p. 1.

3. J. C. Lund (patent pending); For a description of the device, see, for example, reference 3.

4. E. Y. Lee, J. C. Lund, N. R. Hilton, B. A. Brunett, and R. B. James, "Device Simulation of a Unipolar Gamma-Ray Detector," Materials Research Society Symposium Proceedings. Semiconductors for Room-Temperature Radiation Detector Applications II, Vol. **487**, edited by R. B. James, T. E. Schlesinger, P. Siffert, W. Dusi, M. R. Squillante, M. O'Connell, and M. Cuzin (Materials Research Society, Warrendale, Pennsylvania, 1998), p. 537.

5. C. L. Lingren, B. Apotovsky, J. F. Butler, F. P. Doty, S. J. Friesenhahn, A. Oganesyan, B. Pi, S. Zhao, "Mapping Detector Response Over the Area of a CdZnTe-Multiple-Electrode Detector," *Ibid.*, p. 263.

6. P. N. Luke, Appl. Phys. Lett. **65**, 2884(1994).

7. C. Szeles and E. E. Eissler, "Current Issues of High-Pressure Bridgeman Growth of Semi-insulating CdZnTe," Materials Research Society Symposium Proceedings. Semiconductors for Room-Temperature Radiation Detector Applications II, Vol. **487**, edited by R. B. James, T. E. Schlesinger, P. Siffert, W. Dusi, M. R. Squillante, M. O'Connell, and M. Cuzin (Materials Research Society, Warrendale, Pennsylvania, 1998), p. 1.

8. Y. Eisen and A. Shor, "CdTe and CdZnTe Room-Temperature X-Ray and Gamma Ray Detectors and Imaging Systems," *Ibid.*, p. 129.

9. MCNP4B2 is an acronym for Monte Carlo N-Particle Transport Code System. MCNP was prepared by the Regents of the University of California at Los Alamos National Laboratory under contract number W-7405-ENG-36 with the U. S. Department of Energy. It can be obtained from Oak Ridge National Laboratory through Radiation Safety Information Computational Center.

10. SandTMSP V1.0 is copyrighted by the Sandia Corporation (1998).

11. G. Ottoviana, C. Canali, A. A. Quaranta, IEEE Trans. on Nucl. Sci. 22, 192(1975).

12. W. H. Press, S. A. Teukolsky, W. T. Vetterling, B. P. Flannery, Numerical Recipes in C, 2nd edition, Cambridge University Press, New York, 1992, pp. 866.

13. E. Y. Lee and R. B. James, "Device Simulation and Optimization of Laterally-Contacted-Unipolar-Nuclear Detector," Nucl. Inst. And Meth. A (in press).
10. I. K. Andronik and F. M. Lukiyan, Sov. Phys. Semicond. 14, 958(1980).

14. H. W. Yao, R. B. James, E. Y. Lee, R. W. Olsen, H. Hermon, R. J. Anderson, Proceedings of SPIE. Hard X-Ray and Gamma-Ray Detector Physics and Applications, Vol. 3446, 169(1998).

15. P. De Antonis, E. J. Morton, and F. J. W. Podd, IEEE Trans. On Nucl. Sci. 43, 1487(1996).

16. P. N. Luke, M. Amman, T. H. Prettyman, P. A. Russo, and D. A. Close, IEEE Trans. on Nucl. Sci. 44, 713(1997).

Table 1: The best and the worst materials parameters expected for currently commercially available CdZnTe radiation detector materials.

	Materials parameters for the best material	Materials parameters for the worst material
Electron lifetime (μsec)	8	0.73
Hole lifetime (μsec)	0.6	0.06
Electron mobility (cm^2/V/sec)	1100	1000
Hole mobility (cm^2/V/sec)	50	50

Table 2. The active device volumes for the three unipolar devices, for both the best and the worst expected materials parameters given in Table 1. Our definition of the active volume is given in the text. The active volumes are given as percentages of the total detector volumes.

	% active volume for detector having the best material	% active volume for detector having the worst material
LUND	57	23
SpectrumPlus	6	4
Coplanar grid	33	24

List of Figure Captions

Fig. 1. Schematic diagram of the geometry for the device simulations.

Fig. 2. Schematic pictures of the LUND, the SpectrumPlus, and the coplanar grid. A detailed description is given in the text. For the LUND, the guard is shown in gray. For the SpectrumPlus, the anode is black and is at the center, and the guard is in gray. The cathode is located on the opposite face. For the coplanar grid, the two collecting grids are in black and the two noncollecting grids are in gray.

Fig. 3. (a) The relative frequency of occurrence for the scattering events of 662.15 keV gamma-rays interacting with a 5x5x5 mm^3 $Cd_{0.9}Zn_{0.1}Te$ crystal in the geometry shown in Fig. 1. (b) The same as in (a) but counting all events, including the secondary photons.

Fig. 4. (a) The total energy deposited in a 10x10x2 mm^3 CZT crystal in the geometry shown in Fig. 1. The maximum count at the photoelectric peak is 950. (b) The same as (a) but for a 5x5x5 mm^3 CZT crystal. The maximum count at the photoelectric peak is 2300.

Fig. 5. The internal potential field of the unipolar detectors.

Fig. 6. The weighting potentials of the unipolar detectors.

Fig. 7. The charge induced efficiency maps of the unipolar detectors, for the best expected materials.

Fig. 8. The pulse height spectra for the unipolar detectors.

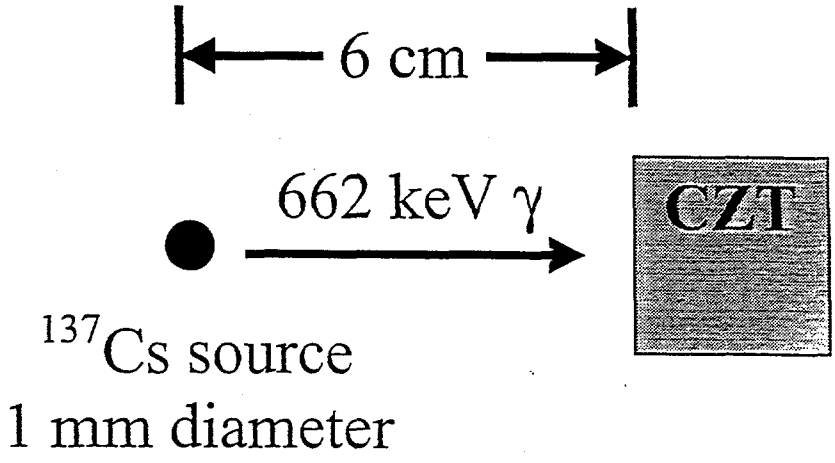

Fig. 1

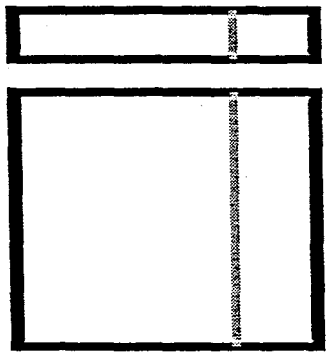

Side view

Top view

LUND

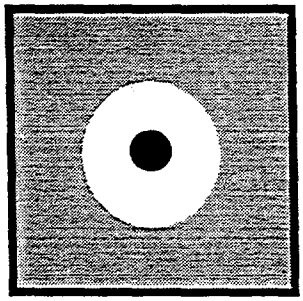

SpectrumPlus

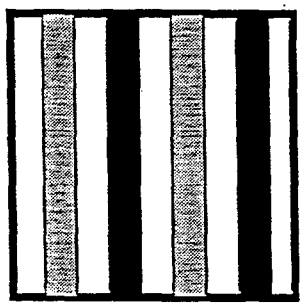

Coplanar

Fig. 2

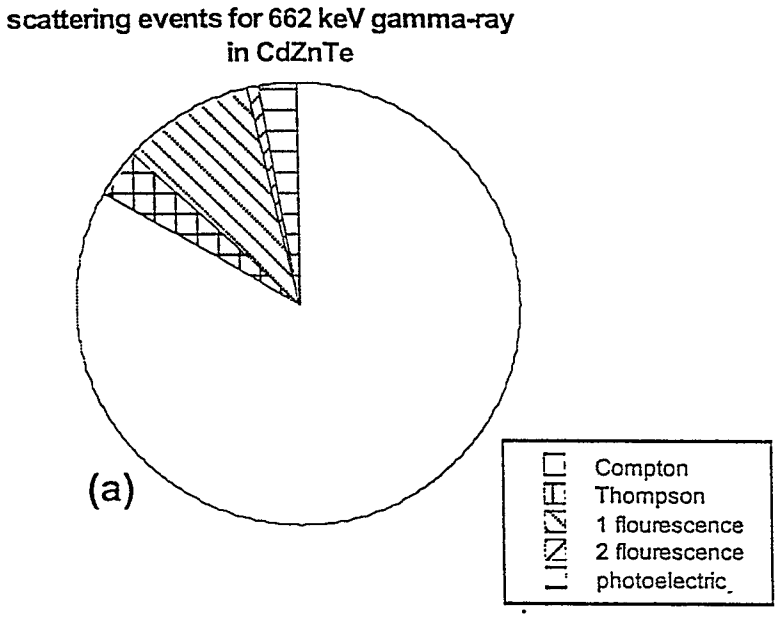
scattering events for 662 keV gamma-ray
in CdZnTe
(a)
Compton
Thompson
1 flourescence
2 flourescence
photoelectric

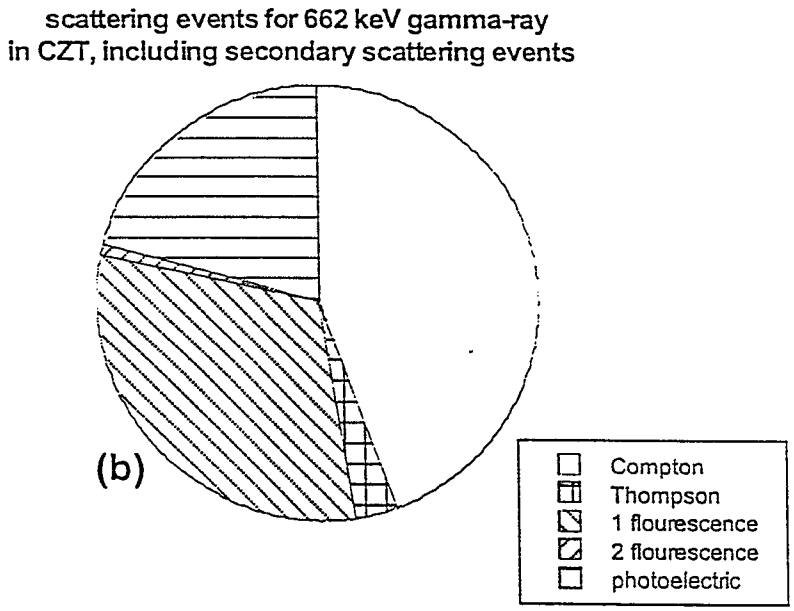
scattering events for 662 keV gamma-ray
in CZT, including secondary scattering events
(b)
Compton
Thompson
1 flourescence
2 flourescence
photoelectric

Fig. 3.

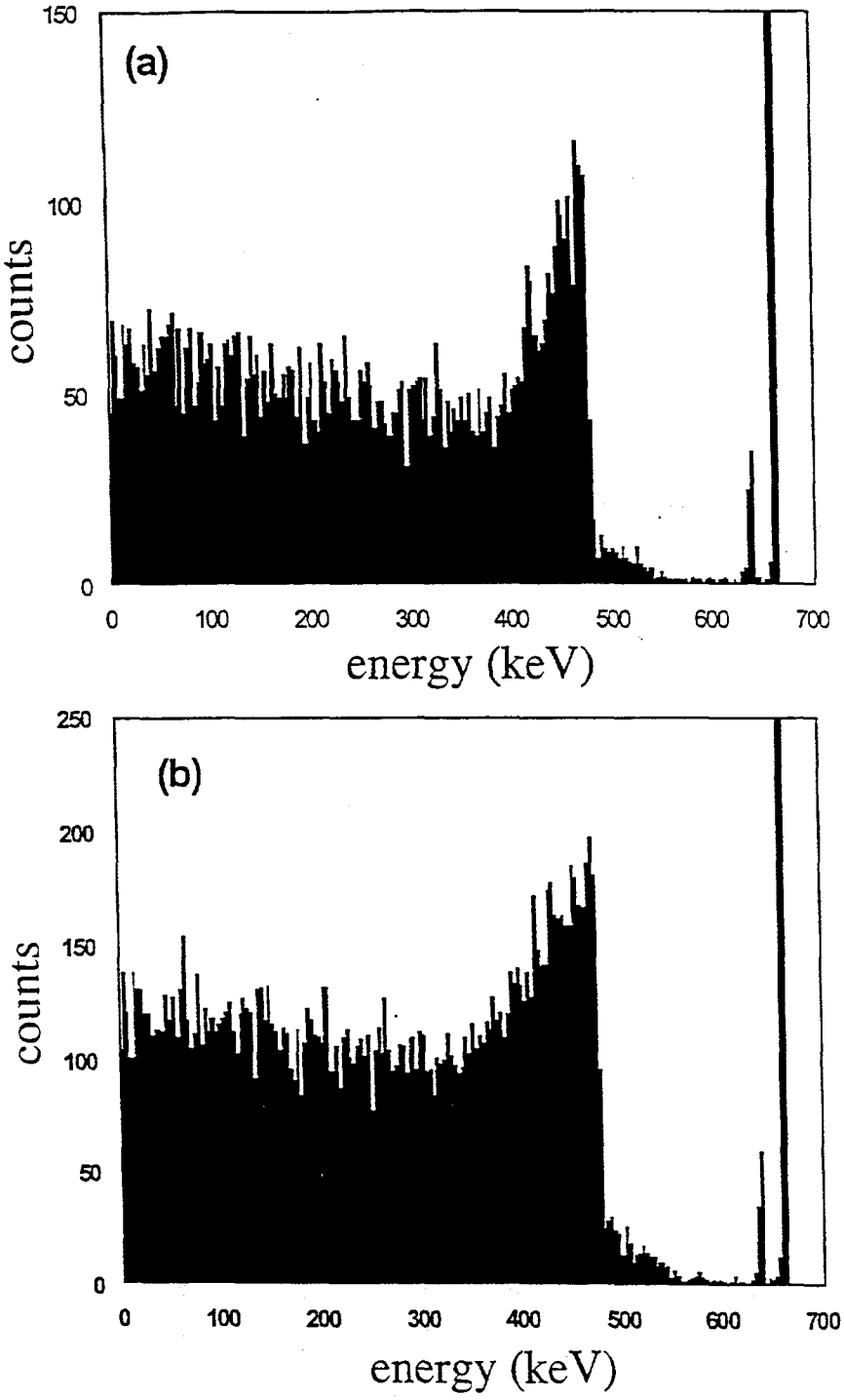
(a)
150
100
50
0
counts
0
100
200
300
400
500
600
700
energy (keV)
(b)
250
200
150
100
50
0
counts
0
100
200
300
400
500
600
700
energy (keV)

Fig. 4

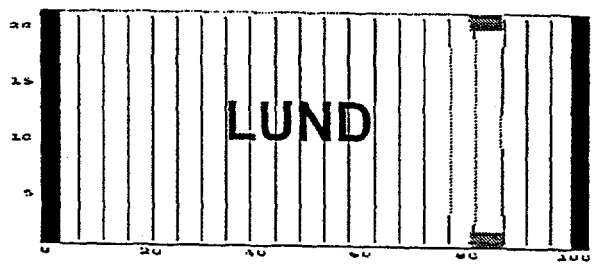

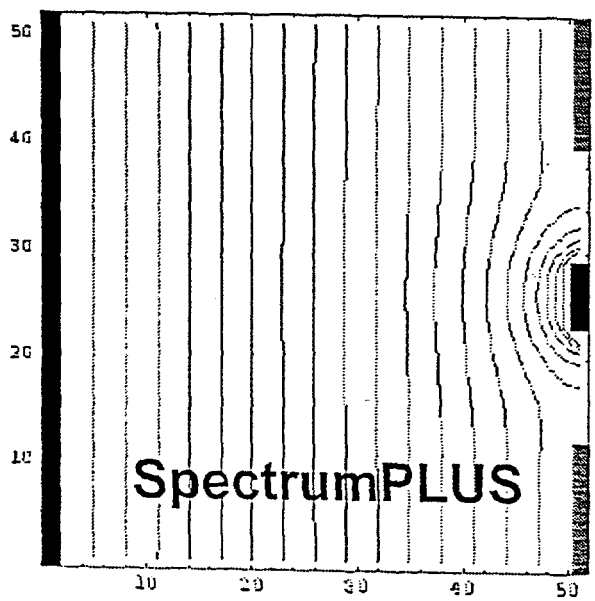

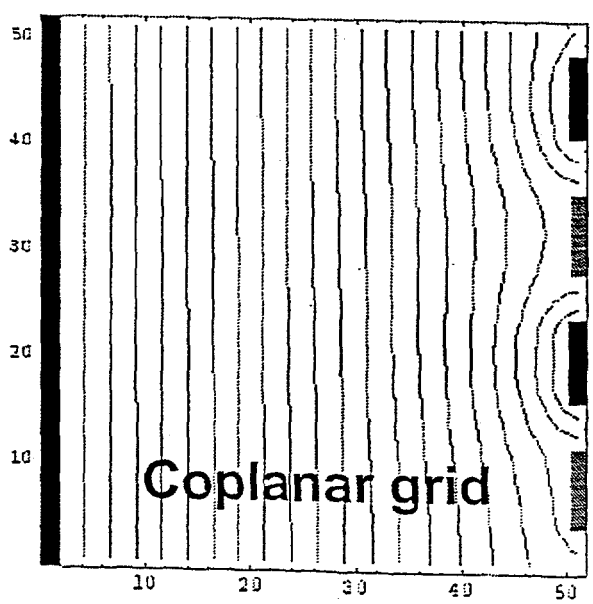

Fig. 5

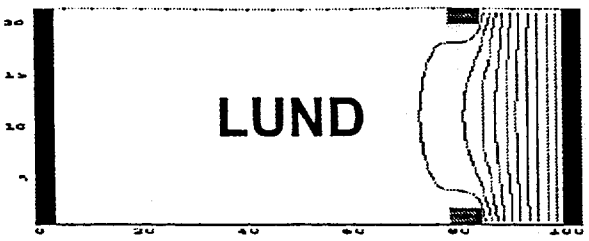
LUND

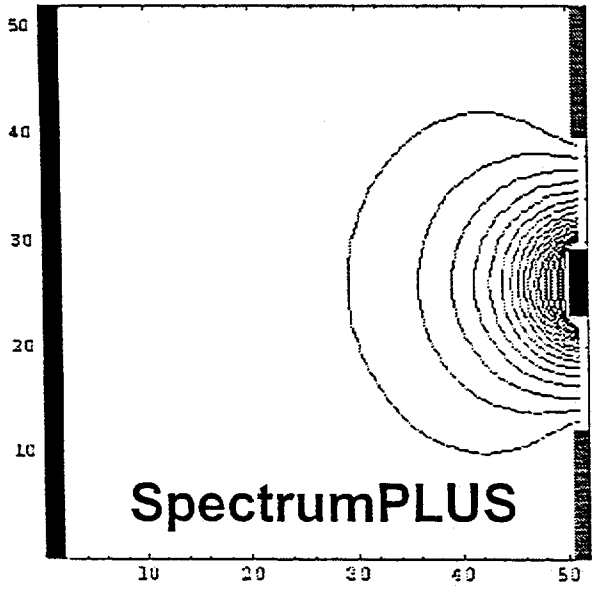
50
40
30
20
10
SpectrumPLUS
10
20
30
40
50

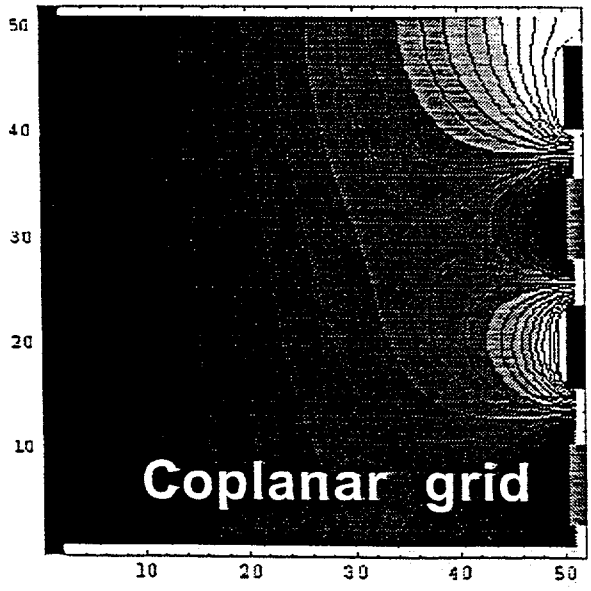
50
40
30
20
10
Coplanar grid
10
20
30
40
50

Fig. 6

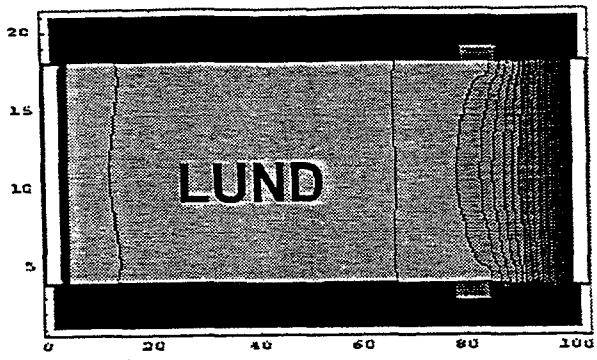
LUND
20
15
10
5
0
20
40
60
80
100

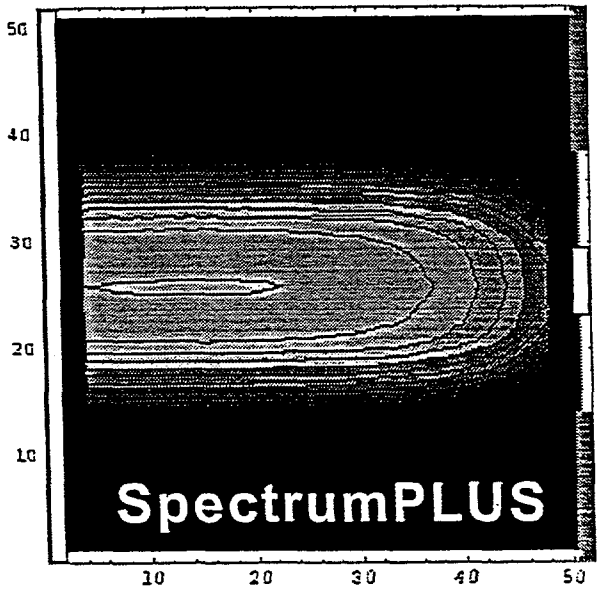
SpectrumPLUS
50
40
30
20
10
10
20
30
40
50

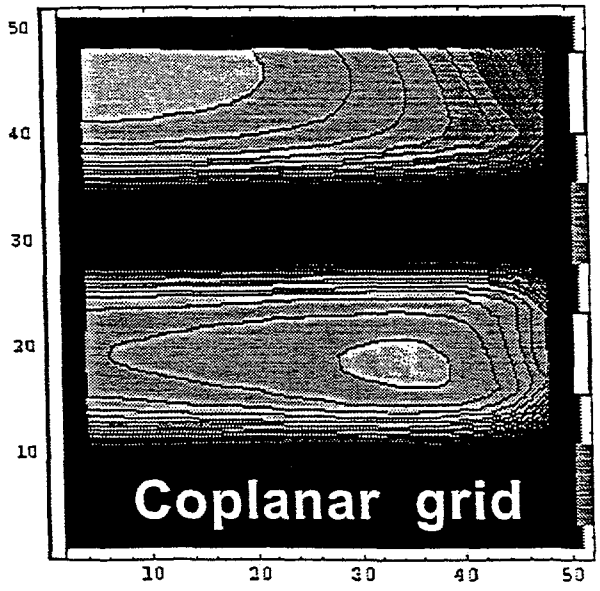
Coplanar grid
50
40
30
20
10
10
20
30
40
50

Fig. 7

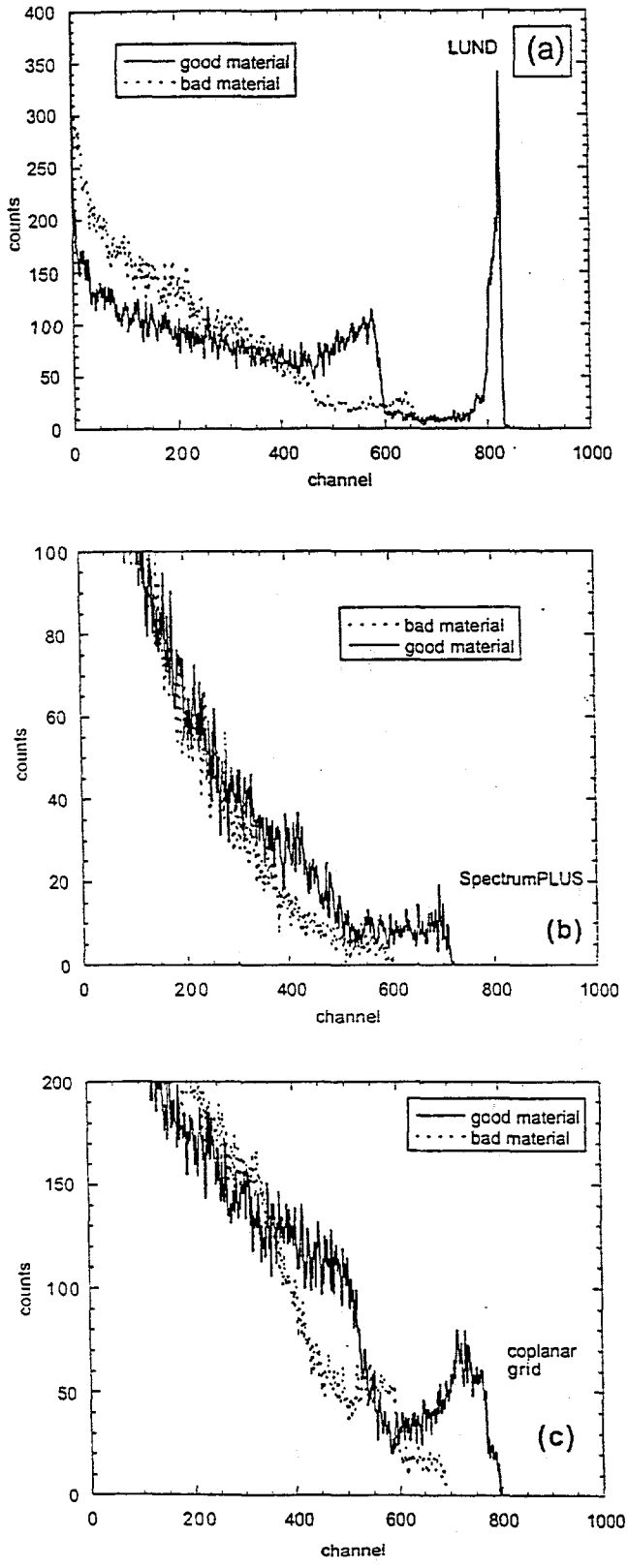
good material
bad material
LUND
(a)
counts
channel
bad material
good material
SpectrumPLUS
(b)
counts
channel
good material
bad material
coplanar
grid
(c)
counts
channel

Fig. 8